ChemComm

Accepted Manuscript

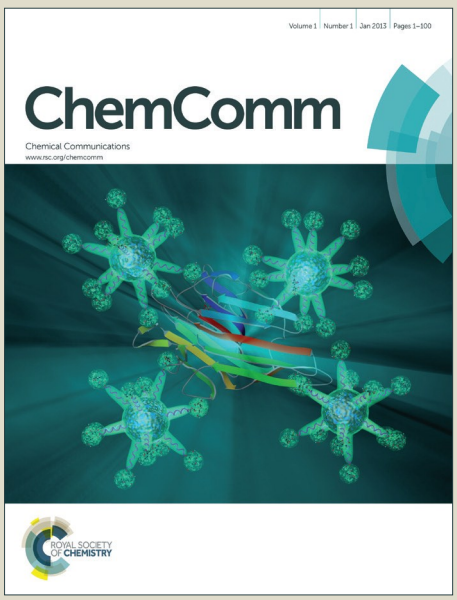

ROYAL SOCIETY OF CHEMISTRY

www.rsc.org/chemcomm

Journal Name

COMMUNICATION

Surfactant-free nickel-silver core@shell nanoparticle in meso-porous SBA-15 for chemoselective hydrogenation of dimethyl oxalate †

Received 00th January 20xx,
Accepted 00th January 20xx

DOI: 10.1039/x0xx00000x

www.rsc.org/

Molly Meng-Jung Li,[a#] Linmin Ye,[b#] Jianwei Zheng,[b] Huihuang Fang,[b] Anna Kroner,[c] Youzhu Yuan,[b*] Shik Chi Edman Tsang[a*]

Surfactant-free bimetallic Ni@Ag nanoparticle in meso-porous silica, SBA-15, is synthesised by simple wet co-impregnation without use of surfactant, which catalyses ultra-chemoselective hydrogenation of dimethyl oxalate to methyl glycolate or ethylene glycol at high yield with no noticeable deactivation: surface analyses and extended X-ray absorption fine structure reveal *ca.* 4.6 nm Ni core-Ag shell structure with strong lattice strain and charge transfer for synergistic catalysis.

Methyl glycolate (MG) and ethylene glycol (EG) are important platform chemicals with broad applications[1-4]. Nowadays, they are mainly produced based on petroleum oil and derivatives. However, diversification of their synthesis based on natural gas, coal or in particular the renewable biomass is becoming important due to dwindling supply of oil and uneven distribution of energy reserves in many different countries. The chemoselective hydrogenation of dimethyl oxalate (DMO) derived from a syngas route may lead to a new non-oil based synthesis procedure for the production of MG and EG[5-11]. Research has shown monometallic Ag catalysts can catalyse mild hydrogenation of DMO to MG and EG[6-9,12], however, low activity and poor stability are the intrinsic problems. In contrast, it is known that the catalytic properties and stability of mono-metallic active phase can be greatly promoted by adding another metal to form bimetallic nanoparticle. The key element in modulating its catalytic performance is the charge transfer (ligand effect) and inducing lattice strain between two metals in small size[13,14]. In general, the use of organic capping agents such as hexadecylamine (HDA) and trioctylphosphine (TOP) can play key roles in the preparation of the small (shaped) bimetallic nanoparticles but these surfactants can affect catalysis and are difficult to remove quantitatively[15]. In our preliminary study, we have demonstrated bimetallic silver-nickel nanoparticles in mesoporous silica support with restricted pore dimension (Ag-Ni/SBA-15) prepared by simple wet co-impregnation of their nitrate precursors without using surfactant are promising for chemoselective hydrogenation of DMO to MG. They displayed 90.6% yield towards MG compared with monometallic Ag (10.1%) or Ni (6.8%) counterparts at 473K[16]. However, the structure and morphology of these mesoporous silica templated Ag-Ni nanoparticles are not yet clear.

In this work, we report the hydrogenation of DMO at higher temperature, 523K over the same catalyst can lead to further quantitative conversion of MG to EG within experimental error (91% EG yield) with no deactivation. This is markedly in contrast with the monometallic Ni counterpart that produces methane as the most favoured product (54.7% CH_4 yield). It is because Ni surface is well known to show a strong propensity for C-O and C-C hydrogenolytic cleavages. In addition, by using surface specific high-sensitivity low-energy ion scattering (HS-LEIS) and X-ray absorption spectroscopy (XAS) technique, no direct exposure of Ni phase is shown. Instead, the Ni phase is in form of core atoms of a small (ca. 4.6± 0.5nm) bimetallic nanoparticle that imposes significant lattice strain to Ag phase in thin Ag shell (ca. 1.1nm). Thus, electronic modulation of Ag shell atoms for superior catalytic performance is concluded. Ag-Ni/SBA-15 catalysts were prepared by a co-impregnation of their nitrate salts to preformed mesoporous silica, see ESI† for details of synthesis of all materials, catalytic activity testing and characterisation techniques.

Table 1 Catalytic performance of Ag-Ni/SBA-15 catalysts for DMO hydrogenation at 473 K[a].

Catalyst	Conversion / %	Selectivity / %				Yield / %
		MG	EG	CH_4	Others[b]	MG
5Ag/SBA-15	10.1	**99.9**	0	0	trace	10.1
$5Ag_1–Ni_{0.05}$/SBA-15	52.1	**98.3**	1.6	0.1	0	51.2
$5Ag_1–Ni_{0.10}$/SBA-15	77.9	**96.7**	3.2	0.1	0	75.3
$5Ag_1–Ni_{0.20}$/SBA-15	97.6	**92.8**	7.0	0.2	0	90.6
$5Ag_1–Ni_{0.40}$/SBA-15	82.9	**96.3**	3.6	0.1	0	79.8
5Ni/SBA-15	10.5	**64.8**	0	35.2	0	6.8

[a] Reaction conditions: $P(H_2)$ = 3.0 MPa, H_2/DMO molar ratio = 80, WLHSV = 1.0 h^{-1}; [b] Others include 1,2-propanediol, 1,2-butanediol, and ethanol.

[a] *Wolfson Catalysis Centre, Department of Chemistry University of Oxford, Oxford, OX1 3QR (UK) Corresponding e-email: edman.tsang@chem.ox.ac.uk;*
[b] *State Key Laboratory of Physical Chemistry of Solid Surfaces, National Engineering Laboratory for Green Chemical Production of Alcohols-Ethers-Esters, iChEM, College of Chemistry and Chemical Engineering, Xiamen University, Xiamen 361005, China. Email: yzyuan@xmu.edu.cn;*
[c] *Diamond Light Source Ltd, Harwell Science and Innovation Campus, Didcot, Oxfordshire, OX11 0DE (UK)*
[#] First author with equal contribution
†Electronic Supplementary Information (ESI) available: Supporting figures, tables, and detailed experimental procedures, including HS-LEIS, XRF, XPS, EXAFS and XRD, etc. See DOI: 10.1039/x0xx00000x

Table 2 Catalytic performance of Ag-Ni/SBA-15 catalysts for DMO hydrogenation at 523 K[a].

Catalyst	Conversion / %	Selectivity / %				Yield / %
		MG	**EG**	CH_4	Others[b]	EG
5Ag/SBA-15	87.3	89.0	**8.9**	0.2	1.9	7.8
$5Ag_1–Ni_{0.05}$/SBA-15	99.1	76.6	**21.8**	0.6	1.0	21.6
$5Ag_1–Ni_{0.10}$/SBA-15	99.0	13.9	**84.8**	0.5	0.8	84.0
$5Ag_1–Ni_{0.20}$/SBA-15	100	7.1	**91.0**	1.0	0.9	91.0
$5Ag_1–Ni_{0.40}$/SBA-15	99.5	5.8	**75.3**	14.6	4.3	74.9
5Ni/SBA-15	99.0	21.0	**18.1**	55.3	5.6	17.9

[a] Reaction conditions: $P(H_2)$ = 3.0 MPa, H_2/DMO molar ratio = 80, WLHSV = 1.0 h^{-1}; [b] Others include 1,2-propanediol, 1,2-butanediol, and ethanol.

Table 1 and Table 2 show the catalytic performance of Ag-Ni/SBA-15 catalysts for DMO hydrogenation at 473K and 523K. It can be seen from Table 1 that MG is the major product when the reaction temperature is at 473K. Adding increasing amount of Ni into the Ag/SBA-15, the DMO conversions are drastically enhanced and progressively reached to a maximum of 97.6% when Ni/Ag is 0.2. It then decreases as the Ni/Ag is 0.4. Compared to monometallic 5Ag/SBA-15 (10.1%) and 5Ni/SBA-15 (6.8%), the $5Ag_1–Ni_{0.20}$/SBA-15 shows much higher yield of MG (90.6%) at 473K.

As demonstrated in Table 2, the incorporation of Ni also shows a positive influence on both DMO conversion and EG selectivity at 523K. As can be seen from Table 2, the DMO conversion increases from 87.3% to 100% with the EG selectivity remarkably enhances from 8.9% to 91% when Ni/Ag=0.2 is used. Further adding Ni has resulted to the decrease of catalytic performance, and become less-selective toward EG. Apparently, $5Ag_1–Ni_{0.20}$/SBA-15 possesses the best performance for DMO hydrogenation reaction among all the monometallic Ag and Ni catalysts and bimetallic Ag-Ni catalysts in this study. This promotive effect can also be shown by TOF analysis in Table S1 and Table S2, (ESI†). The TOF increased as the Ni/Ag increased and reached maximum at $5Ag_1–Ni_{0.20}$/SBA-15, which is in consistent with the trend of catalytic performance presented above.

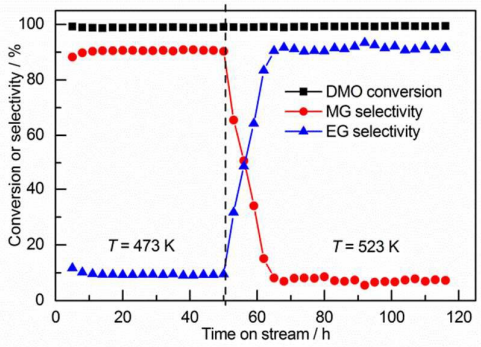

Fig. 1. Stability test of DMO hydrogenation over $5Ag_1–Ni_{0.20}$/SBA-15; reaction conditions: $P(H_2)$ = 3.0 MPa, H_2/DMO molar ratio = 80, WLHSV = 1.0 h^{-1}.

Fig.1 shows the stability test of the DMO hydrogenation reaction over $5Ag_1–Ni_{0.20}$/SBA-15, initially kept at 473K for 50h then raised to 523K until 120h. An interesting product-switching in quantitative manner without producing significant side product, after the reaction temperature was changed from 473K to 523K, is shown. It is also clear that the DMO conversion, MG selectivity at 473K and EG selectivity at 523K were maintained very well during the prolonged testing for 120h, indicative of a good stability for this type of catalysts. As previously noted, Ag catalysts including monometallic Ag/SBA-15 are easy to undergo sintering during DMO hydrogenation reaction hence giving poor catalyst stability[16]. Clearly, the incorporation of a Ni phase improves the stability of Ag atoms from rapid sintering, presumably due to strong affinity of Ag atoms to disperse (known to be poorly miscible to each other) and encapsulate Ni atoms to form thermodynamic stable core-shell structure[17,18].

X-ray photoelectron spectroscopy (XPS) measurements were performed and the result is shown in Fig. 2. The sample was treated in an in situ chamber with 5% H_2-95%N_2 under 693K for 3h prior to the measurements. The Ag 3d XPS spectra of 5Ag/SBA-15 and $5Ag_1–Ni_{0.20}$/SBA-15 samples in Fig. 2A show two strong and distinct peaks at around 367.5eV and 373.5eV attributed as metallic peaks of Ag 3d5/2 and Ag 3d3/2[19]. There are small shoulders of unreduced Ag^+ (368.6eV and 374.6eV) of 5Ag/SBA-15 (a) compared to $5Ag_1–Ni_{0.20}$/SBA-15, reflecting the presence of Ni core to facilitate a complete Ag reduction under the mild reduction conditions[16,20]. Fig. 2B shows corresponding Ni 2p XPS spectra of the two samples. Surprisingly, Ni signals are very weak in $5Ag_1–Ni_{0.20}$/SBA-15 compared to 5Ni/SBA-15, indicating its low surface composition. Table S3 (ESI†) shows the comparison of the Ni/Ag atomic ratios measured by X-ray fluorescence (XRF) with the XPS. The Ni/Ag ratios detected by XPS were substantially less than that obtained by XRF (bulk analysis), which indicates the enrichment of Ag than Ni on the surface as likely to be in core-shell morphology. However, it is known that the photoelectron escaping depth can be penetrated to few nano-meters, thus XPS may still not truly reflect the composition of topmost layer. Therefore a high-sensitivity low-energy ion scattering (HS-LEIS) technique was employed. The HS-LEIS depth profiling of $5Ag_1–Ni_{0.20}$/SBA-15 sample is depicted in Fig. 2C, which indicates the signal of Ni could only be detected when the measured depth was deeper than 1.14nm. As the measured depth increased, the peaks of Ni were getting more obvious. Therefore, Ag is favourable to segregate on the surface of Ag-Ni nanoparticles, while Ni tends to stay in-depth to the core. To further confirm the lack of Ni species on the surface, the experiments of larger scanning area with smaller measured depth were also conducted. Fig. S1 (ESI†) shows the result of scanned range of 1000μm × 1000μm for 7 times (each time for 0.1nm with 0.7nm of total depth), while Fig. S2 (ESI†) shows the result of scanned range of 2000μm × 2000μm for 5 times (each time for 0.02nm with 0.1nm of total depth). No Ni signal was still detected, which confirms the Ni atoms are clearly embedded in core and Ag atoms in shell.

To obtain further information of the local structure of Ag and Ni atoms, X-ray absorption spectroscopy (XAS) was carried out at the Ag K-edge and Ni K-edge. Tables 3 and 4 summarize the extended X-ray absorption fine structure (EXAFS) results. The first shell data analysis has been performed with the systematic errors of coordination number and inter-distance were considered. For the Ag K-edge data, Ag metal with a face centre cubic (fcc) structure was taken as the primary model to generate the scattering path of Ag-Ag. The scattering path was applied to calculate the average number of neighbouring atoms for absorbing Ag. The k3.χ intensity and k3.χ phase corrected Fourier transform fitting curves for the Ag-Ni samples are displayed in Fig. S3 (ESI†). As shown in Table 3, each fitting has an R-factor below 2.1%, and the coordination

number (CN) of Ag atom is found around 7.7 to 8.0 but no Ag-Ni signal can be fitted due to larger scattering parameter and content of Ag. This CN value is typical for 3-5nm nanoparticle with significant numbers of surface non-coordination sites (deviated from CN of 12 of bulk number)[21,22].

Similarly, Table 4 shows the EXAFS fitting result of monometallic Ni/SBA-15 and bimetallic Ag-Ni/SBA-15 samples. Ni metal with an fcc structure was taken as the primary model to generate the scattering path of Ni-Ni for all the samples, while an fcc Ag-Ni model was also taken to generate the scattering path of Ni-Ag for bimetallic samples. The k3.χ intensity and k3.χ phase corrected Fourier transform fitting curves for the Ag-Ni samples are displayed in Fig. S4 (ESI†). As can be seen in Table 4, each fitting has an R-factor below 2.6%. The average coordination number of Ni-Ni in 1Ni/SBA-15 and Ag-Ni/SBA-15 samples is also around 8 indicative of nanoparticle size of the similar size created in SBA-15. However, in the case of Ag-Ni/SBA-15 samples, the additional Ni-Ag coordination signals are evident, giving the total coordination numbers of 12. This high-coordination characteristic of Ag-Ni/SBA-15 samples clearly implies the Ni is in pseudo bulk-like position where the surface unsaturated Ni sites are in contact with Ag atoms in bimetallic core-shell structure, as agreeable to the data from advanced surface analyses (refer to Fig. 2). This observation also matches with general higher CN of core atoms of core-shell structures[23-26].

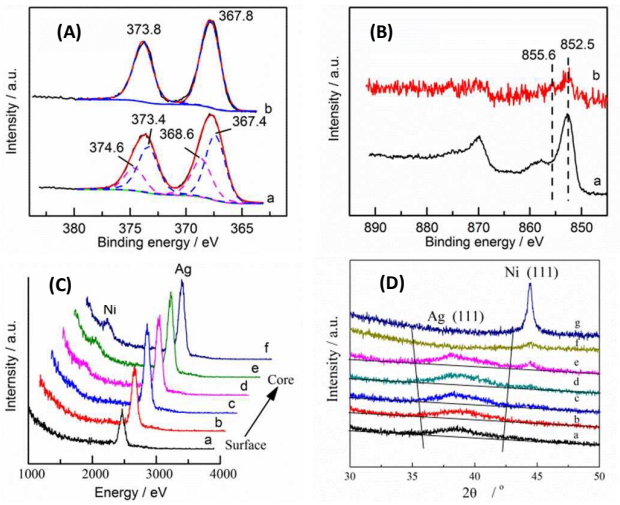

Fig. 2. (A) Ag 3d XPS spectra: (a) 5Ag/SBA-15, (b) $5Ag_1$–$Ni_{0.20}$/SBA-15; **(B)** Ni 2P XPS spectra: (a) 5Ni/SBA-15, (b) $5Ag_1$–$Ni_{0.20}$/SBA-15; **(C)** HS-LEIS of $5Ag_1$–$Ni_{0.20}$/SBA-15: (a) 0.08 nm (b) 0.44 nm (c) 1.14 nm (d) 2.67 nm, (e) 4.20 nm, (f) 7.26 nm; **(D)** XRD showing broadening of Ag(111) peak at higher Ni content: (a) 5Ag/SBA-15, (b) $5Ag_1$–$Ni_{0.05}$/SBA-15, (c) $5Ag_1$–$Ni_{0.10}$/SBA-15, (d) $5Ag_1$–$Ni_{0.20}$/SBA-15, (e) $5Ag_1$–$Ni_{0.40}$/SBA-15, (f) 1Ni/SBA-15 and (g) 5Ni/SBA-15. Ni (111) emerges from (e).

Table 3 Ag K-edge EXAFS for Ag/SBA-15 and Ag-Ni/SBA-15; (Enot is difference in absorption energy between experiment and calculation)

Catalyst	Enot	CN (Ag-Ag)	D-W factor (Ag-Ag)	Bond length (Ag-Ag) / Å	R-factor / %
5Ag/SBA-15	-0.3	8.0(3)	0.013(1)	2.84(1)	1.9
$5Ag_1$–$Ni_{0.20}$/SBA-15	-0.7	7.7(4)	0.014(1)	2.83(1)	2.1
$5Ag_1$–$Ni_{0.40}$/SBA-15	-1.4	7.8(3)	0.014(1)	2.83(1)	2.0

Table 4 Ni K-edge EXAFS for Ni/SBA-15 and Ag-Ni/SBA-15; (Enot is difference in absorption energy between experiment and calculation)

Catalyst	Enot	CN (Ni-Ni)	D-W factor (Ni-Ni)	Bond length (Ni-Ni) / Å	CN (Ni-Ag)	D-W factor (Ni-Ag)	Bond length (Ni-Ag) / Å	R-factor / %
1Ni/SBA-15	-5.1	8.0(4)	0.005(1)	2.48(1)	–	–	–	2.6
$5Ag_1$–$Ni_{0.20}$/SBA-15	-5.6	7.7(3)	0.005(1)	2.48(1)	4.2(6)	0.011(2)	2.78(1)	2.3
$5Ag_1$–$Ni_{0.40}$/SBA-15	-4.8	7.8(3)	0.005(1)	2.48(1)	3.7(5)	0.010(1)	2.79(1)	1.5

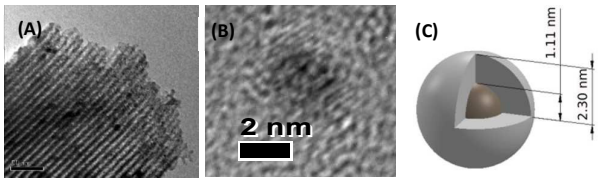

Fig. 3. (A) TEM of encapsulated 4.6±0.5nm NiAg nanoparticles in SBA-15; **(B)** an isolated NiAg core-shell nanoparticle (after removal of SBA-15 silica by NaOH; lattice fringe analysis in Fig. S5); **(C)** calculated 4.6 nm core-shell with 1.11 nm Ag shell thickness according to stoichiometry (ca. 1.14 nm measured by HS-LEIS in Fig. 2C).

From the TEM image an isolated NiAg core-shell nanoparticle can be clearly observed (Fig. 3B). The size of Ni atom is smaller than Ag atom by 16%. This matches with the general observation that the smaller atomic size element resides in the core while the larger comprises the shell due to steric constraints[27,28]. Given that the average particle size of $5Ag_1$–$Ni_{0.20}$/SBA-15 of around 4.6± 0.5nm (Fig. 3(A); restricted the growth by internal pore dimension of the SBA-15 channels), the dimensions of core and shell can be calculated using a simple core-shell sphere model according to mole stoichiometry of Ni and Ag used. Fig. 3(C) summaries the core with 2.3 nm radius, and the thickness of the shell is 1.11 nm. This is in a good agreement with the HS-LEIS data which shows the Ag shell of about 1 nm within error (refer to Fig. 2(C)).

The above structural characterization can explain the fact that the Ni phase in sub-surface lattice as the core in bimetallic nanoparticle will not catalyse the total hydrogenolytic cleavage of the DMO molecules to methane without their extensive surface atoms from direct exposure to the substrate. In our previous characterization we have showed that Ag is somehow activated in the presence of Ni characterised by its lower temperature TPR profile and clear shifts in SPR and CO adsorption peaks[16]. The key question is how the relatively inert Ag atoms of Group IB element on the shell be promoted by the Ni atoms in core-shell nanoparticle to give enhanced ultra-chemoselective hydrogenation of DMO to MG or EG at high yield. The detection of Ag-Ni of intermediate distance (2.78±0.01Å) between larger Ag-Ag distance (2.83±0.01Å) and shorter Ni-Ni distance (2.48±0.01Å) by the EXAFS (Table 3 and Table 4) suggest an intermetallic bonding interface between the two monometallic phases. The differences in atomic size and energy potential of Ni and Ag atoms, there should have lattice mismatches and charge transfer due to difference in d-band energies of two monometallic phases at the interface in Ag-Ni binary core-shell system affecting the fundamental adsorption and catalysis[29]. Ideally, one should expect a compression in Ag lattice exerted by the underlying Ni lattice, which has the same fcc crystal structure as Ni but with a larger lattice parameter (isomorphic effect)[13]. However, we do not anticipate a blunt 'epitaxyl like' interface between the two

metal phases in multifaceted core-shell nanoparticle morphology but rather in the interface region which contains inter-exchanged atoms from both sides, as similar to our previous characterization of CdTe-ZnO nano-interface by atom probe tomography[30]. Besides, the finite solubility (diffusion) between Ni and Ag phases and their difference in thermal expansion coefficient would make somehow irregular interface as contrast from that of single-crystals studies. Indeed, the XRD patterns (Fig. 2(D)) show a significant broadening of the Ag diffraction hump, suggesting both local lattice compression and expansion is taken place after forming the core-shell structure. Apart from the possible lattice strain effects, heterometallic bonding interactions, termed the ''ligand effect'', between Ag atoms of higher band energy and core Ni atoms of lower energy and can result in charge transfer from Ag to Ni, thereby enhancing chemical reactivity of Ag atoms[14]. It is difficult to separate the strain and ligand effects because they occur simultaneously[30,31]. We believe both these strain and ligand effects play the role to activate the Ag shell atoms.

It is noted that we also observed a strong but short range electronic promotion of Ag@Pd bimetallic nanoparticle at catalyst interface whereby using thicker shells of 7-10 atomic Pd layers became much less effective[21]. Thus, synthetic skills to achieve tunable thin layers in core-shell nanocatalyst are important. Using mesoporous SBA-15 as template for particle synthesis, we can accurately control the nanoparticle size therein within 4-5nm without using surfactant. Thus, the rational selection of bimetallic elements according to molar ratio, miscibility, surface energy, diffusion, thermal expansion coefficient, temperature and conditions used may tailor core-shell nanoparticles of optimal geometry and structure for selected catalysis[27,28]. In addition, the 2-D porosity network allows the access of gaseous small substrates and products without much diffusional problems in contrast to that of microporous zeolites. For the $5Ag_1$–$Ni_{0.20}$/SBA-15 with maximum catalytic activity, the 1.1nm Ag shell corresponds to 3 to 4 atomic layers embracing the 2.4nm Ni core. The lower Ni with thicker shell accounts for lower activity but higher Ni results in phase segregation that leads to methane formation. This clearly implies the nano-materials interface within a few atomic distances plays a key role in catalysis. Here we demonstrate the prime importance of careful bimetallic core-shell nanoparticle engineering through controlled nano-synthesis using this mesoporous template in order to obtain the optimum catalysts for this specific catalysis reaction.

In conclusion, the introduction of Ni species into Ag exhibited a strong interaction between Ni and Ag, which shows synergistic effect for enhanced catalytic performance on DMO hydrogenation reaction. When the reaction temperature is at 473K, the yield of MG can be greatly improved from 10.1% to 90.6% by adding Ni into Ag with Ni/Ag=0.2. As the reaction temperature is 523K, the yield of EG can be 91.0% when using $5Ag_1$–$Ni_{0.20}$/SBA-15 as the catalyst, however, the monometallic 5Ag/SBA-15 catalyst only shows 7.8% EG yield. In addition, the $5Ag_1$–$Ni_{0.20}$/SBA-15 presents excellent stability over prolong stability test, which can maintain the conversion and selectivity for at least 120h in our small scale laboratory testing. The local structure of Ag-Ni was also confirmed in this study. It is evident bimetallic Ag-Ni forms a core-shell structure, which generates both geometric and electronic charge transfer effects for the greatly improved catalytic performance in this important reaction.

Notes and references

1. D. He, W. Huang, J. Y. Liu and Q. Zhu, Catal. Today, 1999, 51, 127.
2. D. He, W. Huang, J. Y. Liu and Q. Zhu, J. Mol. Catal. A: Chem., 1999, 145, 228.
3. F. E. Celik, H. Lawrence and A. T. Bell, J. Mol. Catal. A: Chem., 2008, 288, 87.
4. Y. Sun, H. Wang, J. G. Shen, H. C. Liu and Z. M. Liu, Catal. Commun., 2009, 10, 678.
5. H. Yue, Y. Zhao, X. Ma and J. Gong, Chem. Soc. Rev., 2012, 41, 4218.
6. A. Y. Yin, X. Y. Guo, W. L. Dai and K. N. Fan, Chem. Commun., 2010 46, 4348.
7. A. Y. Yin, C. Wen, W. L. Dai and K. N. Fan, Appl. Catal. B: Environ., 2011, 108-109, 90.
8. A. Y. Yin, C. Wen, W. L. Dai and K. N. Fan, J. Mater. Chem., 2011, 21, 8997.
9. J. W. Zheng, H. Q. Lin, Y. N. Wang, X. L. Zheng, X. P. Duan and Y. Z. Yuan, J. Catal., 2013, 297, 110.
10. Z. He, H. Lin, P. He, and Y. Yuan, J. Catal., 2011, 277, 54.
11. A.Y. Yin, X. Y. Guo, W. L. Dai, and K. N. Fan, J. Phys. Chem. C., 2009, 113, 11003.
12. J. W. Zheng, H. Q. Lin, X. L. Zheng, X. P. Duan and Y. Z. Yuan, Catal. Commun., 2013, 40, 129.
13. E. Roduner, Chem. Soc. Rev., 2006, 35, 583.
14. A. Jentys, Phys. Chem. Chem. Phys., 1999, 1, 4059.
15. C. Kim, Y. Kwon and H. Lee, Chem. Commun., 2015, 51, 12316
16. J. Zhou, X. Duan, L. Ye, J. Zheng, M. M. J. Li and S. C. E. Tsang, Appl. Catal. A: Gen., 2015, 505, 344.
17. Z. Y. Zhang, T. M. Nenoff, J. Y. Huang, D. T. Berry and P. P. Provencio, J. Phys. Chem. C, 2009, 113, 1155.
18. M. Gaudry, E. Cottancin, M. Pellarin, J. Lermé, L. Arnaud, J. R. Huntzinger, J. L. Vialle, M. Broyer, J. L. Rousset, M. Treilleux and P. Mélinon, Phys. Rev. B, 2003, 67, 155409.
19. C. D. Wagner, Handbook of X-ray photoelectron spectroscopy, Perkin-Elmer, 1979.
20. A. M. Hengne, A. V. Malawadkar, N. S. Biradar and C. V. Rode, RSC Adv., 2014, 4, 9730.
21. K. Tedsree, T. Li, S. Jones, C. W. A. Chan, K. M. K. Yu, P. Bagot, E. Marquis, G. Smith and S. C. E. Tsang, Nat. Nanotech., 2011, 6, 302.
22. G. Agostini, R. Pellegrini, G. Leofanti, L. Bertinetti, S. Bertarione, E. Groppo, A. Zecchina and C. Lamberti, J. Phys. Chem. C, 2009, 113, 10485.
23. N. Toshima, M. Harada, Y. Yamazaki and K. Asakura, J. Phys. Chem., 1992, 96, 9927.
24. T. Balcha, J. R. Strobl, C. Fowler, P. Dash and R. W. J. Scott, ACS Catal. 2011, 1, 425.
25. F. Liu, D. Wechsler and P. Zhang, Chem. Phys. Lett., 2008, 461, 254.
26. M. R. Knecht, M. G. Weir, A. I. Frenkel and R. M. Crooks, Chem. Mater., 2008, 20, 1019.
27. C. S. Bonifacio, S. Carenco, C. H. Wu, S. D. House and H. Bluhm, J. C. Yang, Chem. Mater., 2015, 27, 6960.
28. G. Pigozzi, D. Mukherji, R. Gilles, P. Jencus and C. Siemers, Nanotechnol., 2009, 20, 245704.
29. J. R. Kitchin, J. K. Norskov, M. A. Barteau and J. G. Chen, Phys. Rev. Lett. 2004, 93, 156801.
30. C. Eley, T. Li, F. Liao, S. M. Fairclough, J. M Smith, G. Smith, and S. C. E. Tsang, Angew Chem. Int. Ed., 2014, 24, 53(30), 7838.
31. W. Tang, and G. Henkelman, J. Chem. Phys. 2009, 130, 194504.